minerals

MDPI

Article

Temperature-Induced Phase Transition in a Feldspar-Related Compound $BaZn_2As_2O_8 \cdot H_2O$

Liudmila A. Gorelova [1,*], Oleg S. Vereshchagin [1], Vladimir N. Bocharov [2], Dmitrii V. Pankin [3] and Tamara Đorđević [4]

[1] Institute of Earth Sciences, Saint Petersburg State University, 199034 St. Petersburg, Russia
[2] Center for Geo-Environmental Research and Modeling (Geomodel), Saint Petersburg State University, 198504 St. Petersburg, Russia
[3] Center for Optical and Laser Materials Research, Saint Petersburg State University, 198504 St. Petersburg, Russia
[4] Institut für Mineralogie und Kristallographie, Universität Wien, 1090 Vienna, Austria
* Correspondence: l.gorelova@spbu.ru

Abstract: The high-temperature (HT) behavior of $BaAs_2Zn_2O_8 \cdot H_2O$ was studied by in situ single-crystal X-ray diffraction (SCXRD) and hot stage Raman spectroscopy (HTRS) up to dehydration and the associated phase transition. During heating, the studied compound undergoes the dehydration process with the formation of $BaAs_2Zn_2O_8$, which is stable up to at least 525 °C. The evolution of the fourteen main Raman bands was traced during heating. The abrupt shift of all Raman bands in the 70–1100 cm^{-1} spectral region was detected at 150 °C, whereas in the spectral region 3000–3600 cm^{-1} all the bands disappeared, which confirms the dehydration process of $BaAs_2Zn_2O_8 \cdot H_2O$. The transition from $BaAs_2Zn_2O_8 \cdot H_2O$ to $BaAs_2Zn_2O_8$ is accompanied by symmetry increasing from $P2_1$ to $P2_1/c$ with the preservation of the framework topology. Depending on the research method, the temperature of the phase transition is 150 °C (HTRS) or 300 °C (HT SCXRD). According to the HT SCXRD data, in the temperature range 25–300 °C the studied compound demonstrates anisotropic thermal expansion ($\alpha_{max}/\alpha_{min}$ = 9.4), which is explained by flexible crankshaft chains of TO_4 (T = As, Zn) tetrahedra. Additionally, we discussed some crystal-chemical aspects of minerals with both (ZnO_n) and (AsO_m) polyhedra (n = 4, 5, 6; m = 3, 4) as main structural units.

Keywords: feldspar; high-temperature; crystal structure; Raman spectroscopy; phase transition; arsenate

Citation: Gorelova, L.A.; Vereshchagin, O.S.; Bocharov, V.N.; Pankin, D.V.; Đorđević, T. Temperature-Induced Phase Transition in a Feldspar-Related Compound $BaZn_2As_2O_8 \cdot H_2O$. *Minerals* **2022**, *12*, 1262. https://doi.org/10.3390/min12101262

Academic Editor: Luca Bindi

Received: 22 September 2022
Accepted: 3 October 2022
Published: 6 October 2022

1. Introduction

Feldspars are one of the most widespread minerals in the Earth's crust. Comprising up to 90 vol. % of magmatic rocks (e.g., anorthosites) their P–T behavior became one of the main focuses of mineralogists and petrologists. Therefore, the major rock-forming minerals related to this group were studied in detail under both ambient and extreme (high pressure (HP) and high-temperature (HT)) conditions (e.g., [1–5]). Other than general information on P–T stability, a number of rare structural units (e.g., SiO_5, BeO_5, PO_5, BeO_6, PO_6, B_2O_6) were discovered in feldspar polymorphs [5–11], which emphasizes the importance of these studies for both Earth sciences and inorganic chemistry.

According to the recent review by Krivovichev [12], there are 29 feldspar-related minerals with the general formula $M[T_4O_8]$ (M = Na, K, Rb, (NH_4), Ca, Sr, Ba; T = Si, Al, B, Be, Zn, As, P, Fe), which could be divided into five groups based on their topology (feldspar, paracelsian, svyatoslavite, dmisteinbergite and hollandite). The crystal structures with feldspar, paracelsian, svyatoslavite and dmisteinbergite topologies are based on the corner-sharing of tetrahedrally coordinated T atoms and hollandite topology based on octahedrally coordinated T atoms. The most widespread minerals of this group relate to the feldspar topology, whereas all other minerals are quite rare.

One of the outstanding examples of feldspar-topology minerals is filatovite $K(Al,Zn)_2(As,Si)_2O_8$ [13]), which is the first example of a natural continuous solid solution series between silicate and arsenate minerals in nature [14]. This mineral was discovered in the fumaroles of the Tolbachik volcano, Kamchatka, Russia [13,15]. Although Vergasova et al. [13] and Filatov et al. [15] reported the chemical formula of filatovite as $K[(Al,Zn)_2(As,Si)_2O_8]$, later research by Shchipalkina et al. [14] showed that the amount of Zn (together with Cu) cannot exceed 1, i.e., the filatovite with $K[(AlZn)As_2O_8]$ composition (most close to the studied here $BaAs_2Zn_2O_8 \cdot H_2O$) is only a hypothetical species. Moreover, filatovite has variable As-content [14], which complicates the study of (AsO_4) behavior in feldspars.

Among natural feldspars, only two contain H_2O groups, namely cymrite $BaAl_2Si_2O_8 \cdot H_2O$ [16] and 'K-cymrite' $KAlSi_3O_8 \cdot H_2O$, the latter of which is described in detail but not approved by the Commission on New Minerals, Nomenclature and Classification [17–20]. Both relate to the dmisteinbergite topology, i.e., they are layered. To date, framework feldspars containing (OH) or H_2O groups are not known in nature. There are only some synthetic compounds with paracelsian topology, containing well-defined H_2O groups ([21], and references therein). Therefore, the high temperature behavior of $BaAs_2Zn_2O_8 \cdot H_2O$ is studied here.

Generally, the study of arsenates minerals is very important due to the high toxicity of arsenic (As), which is an element of concern, owing to its epidemic-like health problems over nearly three decades in southeastern Asia. Although the anthropogenic activities, such as the mining and smelting of sulfide ores, can increase As concentration in the soils, one of its key sources often remains geogenic, because it is one of the main constituents of the parental rocks [22]. The most important problems concerning As bioavailability and its toxicity are closely connected to the stability of As-containing compounds [23], which are very sensitive to the changes in the geochemical environment to more reductive conditions [24]. The decomposition and dissolution of As-containing compounds can lead to the transportation of As into groundwater. Therefore, the study of their temperature behavior and stability is very important.

The aim of the present study was to investigate the structural behavior of $BaAs_2Zn_2O_8 \cdot H_2O$ upon heating and analyze its thermal expansion when compared with other isotypical (or chemically related) minerals and compounds.

2. Materials and Methods

The synthetic sample of $BaAs_2Zn_2O_8 \cdot H_2O$, obtained using synthetic protocol given by Đorđević [21], was used for the high-temperature experiments. It could be considered as zincoarsenate, i.e., a compound isostructural framework of aluminosilicates containing Zn and As exclusively in tetrahedral coordination. Five crystals were chosen for the experiment. Each crystal was checked by single-crystal X-ray diffraction (SCXRD): one was used for the in situ high-temperature (HT) SCXRD experiment and another for the in situ hot-stage Raman spectroscopy (HTRS).

The crystal of $BaAs_2Zn_2O_8 \cdot H_2O$ with approximately the same size 30 × 10 × 10 µm was used for the hot-stage Raman spectroscopy. These experiments were conducted up to 425 °C with the temperature step of 25 °C and at 525 °C. The heating rate was about 25 °C/min. The unpolarized Raman spectra of the sample were recorded from a single crystal using a LabRam HR 800 spectrometer (Horiba Jobin-Yvon, Kyoto, Japan) equipped with a BX-41 (Olympus, Tokyo Japan) microscope and high-temperature attachment THMS600 System (Linkam, UK) in backscattering geometry system using a 532 nm laser. The sample, mounted on a 0.17-mm thick coverslip, was placed on a high-purity polished silver heating element, which guarantees efficient heat transfer as well as very high temperature sensitivity. The resistive platinum sensor ensures the accuracy of the setting and the temperature stability of 0.1 °C. The body of the system is water-cooled for operation at high temperatures. The Raman spectra were recorded in the range of 70–4000 cm^{-1} at a resolution of 1 cm^{-1} and 20 s acquisition time, and the power at the sample was 10 mW. To improve the signal-to-noise ratio, the number of acquisitions was set to 50.

The thermal behavior of $BaAs_2Zn_2O_8 \cdot H_2O$ under heating in the air was studied in situ by HT SCXRD using an XtaLAB Synergy-S diffractometer (Rigaku Oxford Diffraction, Japan) operated with monochromated MoKα radiation (λ[MoKα] = 0.71073 Å) at 50 kV and 40 mA. It was equipped with an HyPix-6000HE detector with a unique high-temperature FMB Oxford system (Oxford, UK). The sample heating was carried out using a gas blower up to 400 (±10) °C. For this experiment, the needle-like single crystal with the approximate size of 30 × 10 × 10 μm was mounted on the glass fiber, which was placed into the quartz capillary. Diffraction data were collected at different temperatures without changing the orientation of the crystal in the range of 27 to 300 °C with a temperature step of 50 °C. The crystal was also heated up to 400 °C, but due to the experimental features, the SCXRD data were not collected at this temperature—instead, they were collected at 27 °C after cooling. The data were integrated and corrected for background, Lorentz, and polarization effects. An empirical absorption correction based on the spherical harmonics implemented in the SCALE3 ABSPACK algorithm was applied in the CrysAlisPro program 171.37.35 [25]. The unit-cell parameters were refined using the least-square techniques. The SHELXL program package [26] was used for all structural calculations. The structure model of $BaAs_2Zn_2O_8 \cdot H_2O$ by Đorđević [21] was used as a starting model for structure refinements. The crystallographic information files (CIFs) for the crystal structures at all temperatures can be found as Supplementary Materials.

The temperature dependencies of the unit-cell parameters were described by quadratic and linear (for comparison with other minerals) polynomial functions in the whole temperature range (see below for more details). Based on these data, the thermal expansion coefficients were determined using the TTT program package [27]. This program package has also been used for the thermal-expansion parameter tensor visualization.

3. Results

3.1. Raman Spectra Evolution of $BaAs_2Zn_2O_8 \cdot H_2O$ upon Heating

The Raman spectrum of $BaAs_2Zn_2O_8 \cdot H_2O$ under ambient conditions (Figure 1a) is in a good agreement with the published data [21]. The bands in the regions from 800 to 1000 cm^{-1} correspond to the stretching vibrations of AsO_4 only, whereas the bands from 350 to 550 cm^{-1} correspond to stretching vibrations of ZnO_4 groups and the bending modes of the AsO_4 groups, respectively. In the low-frequency region (below 350 cm^{-1}), various lattice modes of the compound appear. In the high frequency region (3000–3600 cm^{-1}) there are two bands at 3465 and 3271 cm^{-1}, which correspond to the O–H stretching vibrations of the H_2O molecule, but in contrast to the spectrum by Đorđević [21], the band at 3271 cm^{-1} has a very weak intensity.

A detailed study of the evolution of the Raman spectra of $BaAs_2Zn_2O_8 \cdot H_2O$ on heating from 27 to 525 °C showed a phase transition at 150 °C (Figure 1b,c and Figure 2). The most important changes are in the high-frequency region (3000–3600 cm^{-1}), where all peaks disappear at the temperature above 150 °C (Figure 1c), which relates to the dehydration process. Moreover, the Raman spectrum in the low-frequency region (from 70 to 1000 cm^{-1}) is changed significantly as well: the evolution of 14 Raman bands in this region was traced during heating (Figures 1b and 2). In general, all of the Raman bands, except ν_{11} of the studied compound, move to lower wavenumbers, i.e., undergo a red shift. However, abrupt changes of almost all bands occur between 125 and 150 °C: some of them shift significantly; some of them appear or disappear. These changes indicate the phase transition from $BaAs_2Zn_2O_8 \cdot H_2O$ to $BaAs_2Zn_2O_8$, which is most probably accompanied by symmetry increasing. It should be noted that the band at about 509–520 cm^{-1} (depending on temperature) undergoes a blue shift between 125 and 150 °C. As this band is associated with the ZnO_4 group, the unusual moving of this band can be explained by the distortion of the ZnO_4 tetrahedra in the crystal structure of $BaAs_2Zn_2O_8$ (see below), which is typical for a ZnO_4 tetrahedra comparison with AsO_4 [21,28].

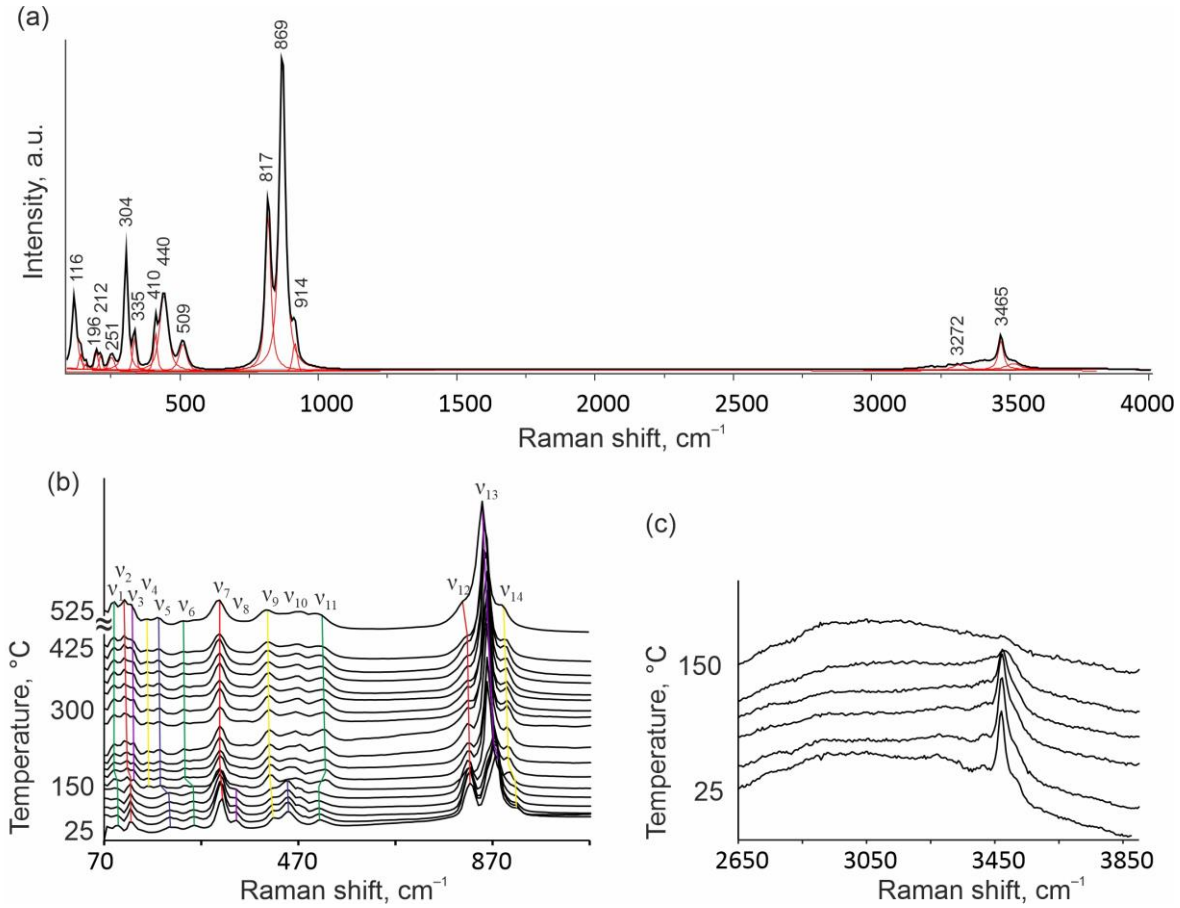

Figure 1. Raman spectra of $BaAs_2Zn_2O_8 \cdot H_2O$ under ambient conditions from 70 to 4000 cm^{-1} (**a**); at different temperatures from 70 to 1070 cm^{-1} (**b**) and from 2650 to 3850 cm^{-1} (**c**).

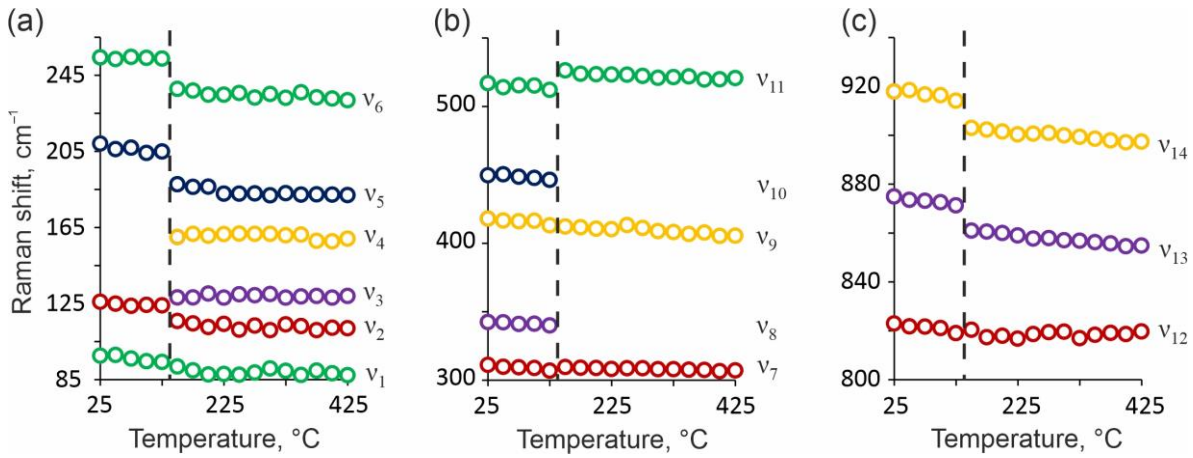

Figure 2. Temperature evolution of some selected Raman bands from 85 to 265 cm^{-1} (**a**), from 300 to 550 cm^{-1} (**b**), and from 800 to 940 cm^{-1} (**c**). The broken vertical lines demonstrate the abrupt changes in the temperature evolution of the Raman bands. The errors are smaller than the size of the symbols.

3.2. Crystal Structure Evolution of $BaAs_2Zn_2O_8 \cdot H_2O$ upon Heating

The crystal structure of the studied sample was refined at eight temperature points (Tables 1 and 2), including room temperature (ambient conditions) after cooling. The positions of H atoms could not be determined due to their low scattering power and the features of the high-temperature experiments. Anisotropic displacement parameters were refined for all atoms, except O1 and O5 atoms at 50 and 100 °C, respectively.

Table 1. Crystallographic data and refinement parameters for $BaZn_2As_2O_8 \cdot H_2O$ at different temperatures and $BaZn_2As_2O_8$ at room temperature (T07).

Temperature, °C	**27**	**50**	**100**	**150**	**200**	**250**	**300**	**23**
	T00	**T01**	**T02**	**T03**	**T04**	**T05**	**T06**	**T07**
Space group				$P2_1$				$P2_1/c$
a, Å	5.2854 (4)	5.2840 (3)	5.2882 (3)	5.2918 (3)	5.2957 (3)	5.2986 (3)	5.3037 (4)	8.8073 (11)
b, Å	10.3919 (8)	10.3901 (5)	10.3940 (5)	10.3948 (6)	10.3964 (6)	10.3948 (6)	10.3959 (7)	9.9861 (11)
c, Å	8.0394 (7)	8.0347 (5)	8.0395 (5)	8.0425 (5)	8.0451 (5)	8.0462 (5)	8.0483 (6)	9.4060 (11)
β, °	95.445 (8)	95.359 (5)	95.346 (5)	95.309 (5)	95.262 (6)	95.263 (6)	95.285 (7)	91.471 (10)
Volume, Å^3	439.58 (6)	439.19 (4)	439.97 (4)	440.49 (4)	441.07 (5)	441.30 (5)	441.87 (5)	826.99 (17)
Z				2				2
	Data collection							
Wavelength, Å				0.71073				0.71073
Max. θ°	31.672	29.300	29.285	29.280	29.355	29.360	29.486	33.799
Index ranges	$-7 \le h \le 7$ $-14 \le k \le 15$ $-9 \le l \le 11$	$-7 \le h \le 4$ $-14 \le k \le 13$ $-10 \le l \le 10$	$-7 \le h \le 4$ $-14 \le k \le 13$ $-10 \le l \le 10$	$-7 \le h \le 4$ $-14 \le k \le 13$ $-10 \le l \le 10$	$-4 \le h \le 7$ $-14 \le k \le 14$ $-10 \le l \le 10$	$-4 \le h \le 7$ $-14 \le k \le 14$ $-10 \le l \le 10$	$-7 \le h \le 4$ $-13 \le k \le 14$ $-10 \le l \le 11$	$-13 \le h \le 13$ $-15 \le k \le 14$ $-14 \le l \le 14$
No.meas.refl.	5422	4853	4848	4879	4383	4883	4635	10016
No.uniq.refl.	2356	2033	2034	2040	1997	2026	2061	2957
No.obs.refl ($I > 2\sigma(I)$)	2083	1755	1728	1709	1570	1650	1577	1319
	Refinement of the structure							
No. of variables	128	123	123	128	128	128	128	118
R_{int}	0.0657	0.0480	0.0495	0.0495	0.0585	0.0533	0.0525	0.1495
R_1, all data	0.0526	0.0507	0.0526	0.0540	0.0617	0.0606	0.0706	0.2347
R_1, $I > 2\sigma(I)$	0.0443	0.0388	0.0381	0.0399	0.0410	0.0423	0.0459	0.1052
wR_2, all data	0.0965	0.0692	0.0680	0.0691	0.0651	0.0779	0.0801	0.2999
wR_2, $I > 2\sigma(I)$	0.0938	0.0664	0.0637	0.0657	0.0608	0.0725	0.0739	0.2259
GooF	0.990	1.015	1.007	1.004	0.945	1.009	1.011	1.031

The crystal structure of $BaAs_2Zn_2O_8 \cdot H_2O$ is monoclinic with the $P2_1$ space group [21] under ambient conditions (before cooling). It relates to the feldspar-type structures with the paracelsian topology, i.e., the crystal structure is based on a three-dimensional tetrahedral framework and consists of four- and eight-membered rings of alternate corner-sharing ZnO_4 and AsO_4 tetrahedra. The cavities of the eight-membered rings are occupied by Ba atoms coordinated by eight oxygen atoms and H_2O groups, which are bonded only to Ba atoms (Table 2, Figure 1a). Though the framework topology of $BaAs_2Zn_2O_8 \cdot H_2O$ relates to the paracelsian, due to the existence of H_2O groups, its crystal structure has lower symmetry and is not identical with the danburite- and paracelsian-like compounds.

The diffraction pattern of studied crystal changed dramatically after heating above 300 °C: the quality of the SCXRD data deteriorated significantly, which is reflected in the intensity decrease and transformation of the single crystal into a polycrystalline sample. It was impossible to perform an SCXRD experiment for this sample at 400 °C due to the features of the high-temperature experiment (large distance from the crystal to the detector and the lower frame intensities as a consequence). Only a pre-experiment, allowing the unit-cell parameters to be determined, was performed at these temperatures. Thus, after heating up to 400 °C, the studied sample was cooled to 27 °C and the full SCXRD data were collected in "normal" geometry.

It was found that the crystal structure of $BaAs_2Zn_2O_8 \cdot H_2O$ undergoes the dehydration process at a temperature above 300 °C. This process is accompanied by symmetry increasing from $P2_1$ to $P2_1/c$ (Figure 3, Table 1). The resulting phase transition is irreversible, which is confirmed by the similarity of the unit-cell parameters obtained at 400 and 27 °C (crystal data after cooling). The crystal structure of anhydrous phase $BaAs_2Zn_2O_8$ preserves the initial paracelsian topology, but the framework becomes more symmetric. The cavities of the eight-membered rings in the anhydrous phase are occupied by Ba atoms only, whereas in the hydrated phase they are occupied by both Ba and H_2O. Previously, this phase was synthesized by Lucas et al. [28,29], who refined its crystal structure using the Rietveld refinement method. Moreover, this phase crystallizes as the major phase in the synthesis of $BaAs_2Zn_2O_8 \cdot H_2O$ [21].

Table 2. Bond distances and polyhedral parameters in $BaZn_2As_2O_8 \cdot H_2O$ at different temperatures.

Temperature, °C	23	50	100	150	200	250	300
	T00	T01	T02	T03	T04	T05	T06
				AsO_4 tetrahedra			
As1–O2 (Å)	1.680 (12)	1.672 (11)	1.682 (11)	1.679 (12)	1.662 (12)	1.675 (12)	1.676 (14)
As1–O4 (Å)	1.691 (11)	1.679 (10)	1.675 (12)	1.669 (11)	1.686 (12)	1.684 (13)	1.677 (13)
As1–O5 (Å)	1.674 (10)	1.695 (10)	1.701 (10)	1.681 (10)	1.700 (11)	1.691 (11)	1.679 (12)
As1–O6 (Å)	1.678 (10)	1.670 (9)	1.670 (10)	1.662 (10)	1.672 (10)	1.672 (11)	1.651 (11)
<As1–O> (Å)	1.681	1.679	1.682	1.673	1.680	1.681	1.670
Volume (Å^3)	2.436	2.428	2.441	2.401	2.434	2.435	2.390
As2–O1 (Å)	1.678 (12)	1.684 (12)	1.685 (11)	1.683 (12)	1.685 (12)	1.686 (12)	1.680 (13)
As2–O3 (Å)	1.681 (12)	1.670 (11)	1.667 (11)	1.664 (11)	1.680 (12)	1.663 (13)	1.671 (13)
As2–O7 (Å)	1.688 (11)	1.686 (10)	1.674 (10)	1.679 (10)	1.691 (10)	1.664 (11)	1.684 (12)
As2–O8 (Å)	1.667 (11)	1.672 (11)	1.660 (11)	1.675 (12)	1.660 (12)	1.658 (13)	1.661 (13)
<As2–O> (Å)	1.678	1.678	1.672	1.675	1.679	1.668	1.674
Volume (Å^3)	2.424	2.423	2.395	2.411	2.428	2.380	2.408
				ZnO_4 tetrahedra			
Zn1–O1 (Å)	1.975 (12)	1.980 (12)	1.979 (11)	1.979 (12)	1.972 (12)	1.977 (12)	1.982 (13)
Zn1–O3 (Å)	1.953 (11)	1.964 (11)	1.965 (11)	1.965 (11)	1.959 (12)	1.960 (13)	1.964 (13)
Zn1–O5 (Å)	1.935 (10)	1.929 (9)	1.922 (9)	1.931 (9)	1.935 (10)	1.926 (10)	1.931 (11)
Zn1–O6 (Å)	1.903 (12)	1.909 (11)	1.910 (12)	1.913 (13)	1.882 (13)	1.895 (14)	1.909 (14)
<Zn1–O> (Å)	1.942	1.946	1.944	1.947	1.937	1.939	1.946
Volume (Å^3)	3.645	3.667	3.655	3.676	3.614	3.627	3.661
Zn2–O2 (Å)	1.968 (11)	1.969 (11)	1.961 (11)	1.971 (12)	1.974 (12)	1.967 (13)	1.969 (13)
Zn2–O4 (Å)	1.955 (11)	1.968 (10)	1.955 (12)	1.959 (11)	1.945 (13)	1.948 (13)	1.959 (13)
Zn2–O7 (Å)	1.941 (12)	1.934 (11)	1.935 (12)	1.938 (12)	1.947 (12)	1.949 (13)	1.947 (14)
Zn2–O8 (Å)	1.934 (10)	1.940 (10)	1.941 (10)	1.934 (10)	1.935 (11)	1.939 (11)	1.936 (11)
<Zn2–O> (Å)	1.949	1.953	1.948	1.951	1.950	1.951	1.953
Volume (Å^3)	3.699	3.723	3.702	3.711	3.701	3.709	3.711
				BaO_8 polyhedra			
Ba–O1 (Å)	2.726 (11)	2.715 (10)	2.723 (10)	2.728 (11)	2.728 (11)	2.725 (11)	2.734 (12)
Ba–O2 (Å)	2.770 (13)	2.774 (11)	2.783 (11)	2.778 (12)	2.794 (12)	2.789 (12)	2.785 (14)
Ba–O3 (Å)	2.697 (11)	2.702 (9)	2.708 (9)	2.711 (10)	2.701 (11)	2.726 (11)	2.711 (11)
Ba–O4 (Å)	2.761 (10)	2.763 (10)	2.781 (11)	2.782 (11)	2.781 (12)	2.783 (12)	2.787 (12)
Ba–O5 (Å)	2.902 (10)	2.879 (10)	2.880 (11)	2.897 (11)	2.874 (12)	2.888 (12)	2.896 (13)
Ba–O7 (Å)	2.744 (11)	2.752 (11)	2.756 (11)	2.761 (12)	2.736 (11)	2.766 (12)	2.746 (14)
Ba–O9 (Å)	2.897 (11)	2.905 (9)	2.912 (10)	2.916 (10)	2.904 (11)	2.924 (11)	2.908 (12)
Ba–O9 (Å)	2.985 (11)	2.971 (10)	2.988 (11)	2.980 (11)	2.999 (11)	3.000 (12)	3.010 (13)
<Ba–O> (Å)	2.810	2.808	2.816	2.819	2.815	2.825	2.822
Volume (Å^3)	36.106	36.119	36.322	36.461	36.245	36.606	36.465

The comparison of the Raman spectra obtained during the in situ high-temperature experiment and the spectrum obtained from the cooled crystal, which was heated during the SCXRD experiment, demonstrates their similarity (Figure 4). In both cases there are no Raman bands in the high frequency region (3000–3600 cm^{-1}), which confirms the dehydration state of the compound for the cooled sample. All existing bands between 70 and 1000 cm^{-1} are similar and corrected for the shift caused by different temperatures. Moreover, it is one more confirmation that $BaAs_2Zn_2O_8$ is a quenchable phase.

The significant difference in the dehydration temperatures obtained by the SCXRD (300 °C) and Raman (150 °C) experiments cannot be explained with certainty. As mentioned above, the error for each of the methods does not exceed 10 °C. Therefore, the possible reasons for the obtained results could be: (1) the process kinetics, which are associated with

the different crystal size and the speed of the heating; (2) a variable amount of H_2O groups in different crystals.

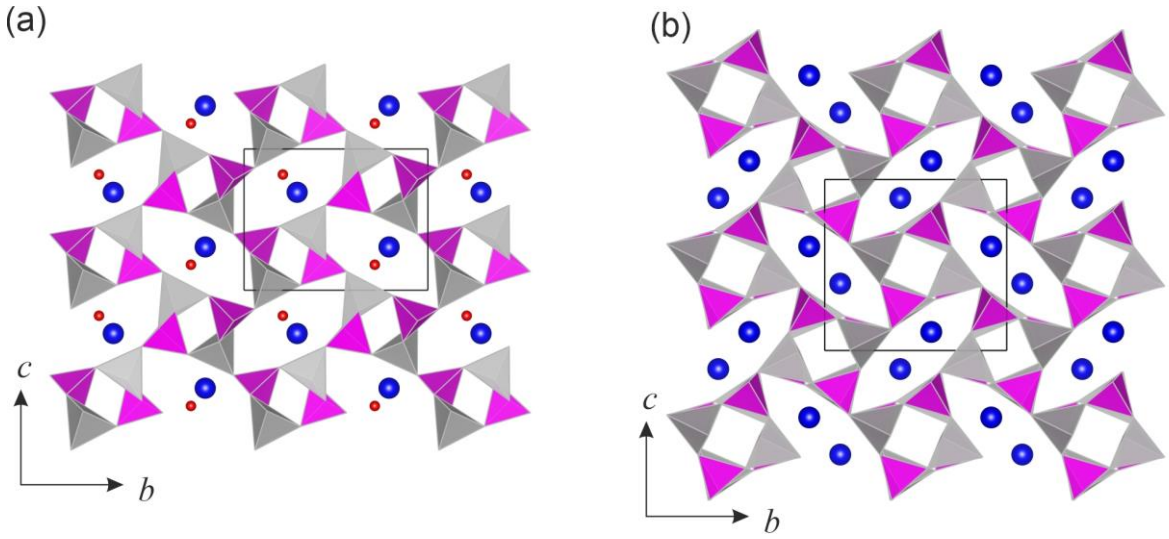

Figure 3. Crystal structure of $BaAs_2Zn_2O_8 \cdot H_2O$ (**a**) and $BaAs_2Zn_2O_8$ (**b**) under ambient condition. AsO_4 and ZnO_4 tetrahedra are given in purple and grey, respectively. Ba and O atoms are presented as blue and red spheres, respectively.

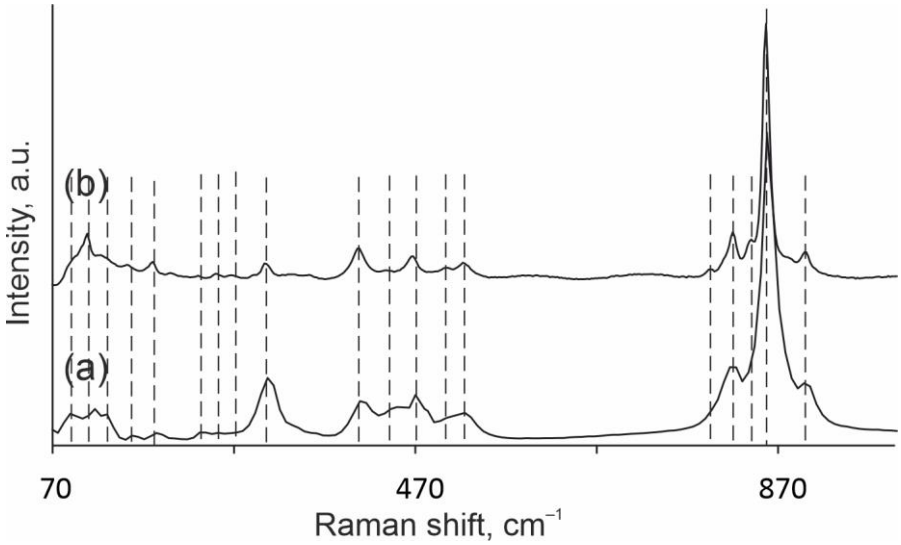

Figure 4. Raman spectra of $BaAs_2Zn_2O_8$ at 175 °C, obtained during in situ high-temperature Raman experiment (a) and at 27 °C from the crystal, which has been studied by high-temperature SCXRD (b).

The relation between H_2O content, unit-cell parameters and phase stability has been previously discovered in calcium oxalates [30–32]. According to these studies, the amount of H_2O in weddellite crystal structure can vary, and the end-membered formula should be written as $CaC_2O_4 \cdot (2.5–x)H_2O$, where $0 \leq x \leq 0.25$. Izatulina et al. [30] noted that there is a positive correlation between H_2O content and the *a* parameter. She suggested to use this for the precise determination of the H_2O content. However, verification of the unit-cell parameters of five crystals of $BaAs_2Zn_2O_8 \cdot H_2O$ under ambient conditions does not reveal any significant and regular variations. From crystal to crystal, the changes of the unit-cell parameters vary by ~0.01–0.03 Å, which is more than the error of their nominal determination but is close to the real error for the single crystal data [33].

Consequently, the most probably difference between HTRS and HT SCXRD data is connected to the experimental features of each of the methods. The most important aspects influencing the kinetic process are preparative routine, environmental conditions, the heating rate and the presence and nature of the flowing gas [32,34–40]. The most reliable results derive from the experiments with the low mass and slow heating rate [41,42], but not always [38]. In our case, the size of the studied crystals was approximately the same, but the heating method and sample preparation were different. This is a potential explanation for such a great difference in the temperature of the dehydration process.

The dehydration of other Zn- and As-containing compounds with zeolitic water usually occurred at ~100–200 °C, depending on the initial crystal structure, chemical composition and speed of heating, e.g., $Na_3Zn_4O(AsO_4)_3 \cdot 6H_2O$ lose all H_2O groups at 150 °C [43], whereas the dehydration of $Cs_2(ZnAsO_3OH)(ZnAsO_4)_2 \cdot H_2O$ occurred at 200 °C [44]. Moreover, $BaAs_2Zn_2O_8$ was the main phase in the synthesis of $BaAs_2Zn_2O_8 \cdot H_2O$ Đorđević [21], which was conducted at temperatures below 220 °C.

3.3. Thermal Expansion of $BaAs_2Zn_2O_8 \cdot H_2O$

The temperature dependencies of the unit-cell parameters obtained during the SCXRD experiment are shown in Figure 5. The changes of the unit-cell parameters are relatively linear in the temperature range from 27 to 300 °C. Therefore, no phase transition was supposed. The crystal structure refinements confirm the absence of phase transition or dehydration process at the temperatures below 300 °C (Tables 1 and 2). According to SCXRD data, the site of the O atom belonging to a H_2O molecule (namely, the O9 atom) is clearly defined.

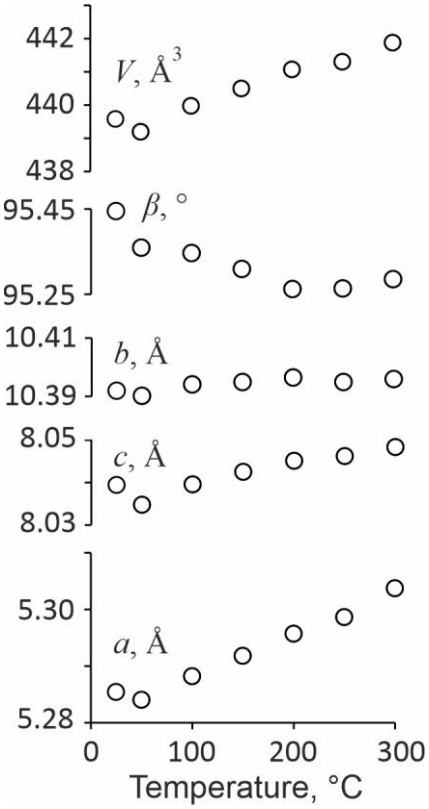

Figure 5. The temperature-induced evolution of the unit-cell parameters (*a*, *b*, *c*, *β* and *V*) of $BaAs_2Zn_2O_8 \cdot H_2O$. The errors are smaller than the size of the symbols.

Thermal expansion coefficients (TECs) calculated with the linear approximation of the unit-cell parameters' temperature dependencies are the following: α_{11} = 16.0(8), α_{33} = 3.5(9), $\mu(\alpha_{33}\hat{}c)$ = 22.6(6), α_a = 13.2(9), $\alpha_b = \alpha_{22}$ = 1.7(5), α_c = 5.3(9), α_β = –6(2),

α_V = 21(1) $\times 10^6$ °C^{-1}. The thermal expansion of $BaAs_2Zn_2O_8 \cdot H_2O$ has an extremely anisotropic character: $\alpha_{max}/\alpha_{min}$ = 9.4. The maximum and minimum expansion was observed practically along the *a* and *b* axes, respectively (Figures 5 and 6). Thus, the direction of the maximal thermal expansion is along the flexible crankshaft chains and can be explained by their straightening, which is typical for feldspar-related compounds with feldspar topology [45]. The expansion of the pseudo-layer (*bc* plane) is more isotropic (α_c/α_b = 3.1) but, compared with other feldspar-related compounds, is still anisotropic. Such expansion in this plane was previously observed for another feldspar-related compound with paracelsian topology, maleevite $BaB_2Si_2O_8$ [46], wherein its Sr and Ca analogues did not demonstrate sharp anisotropy. This phenomenon was explained by hinge deformations [47] of the four-fold rings [46].

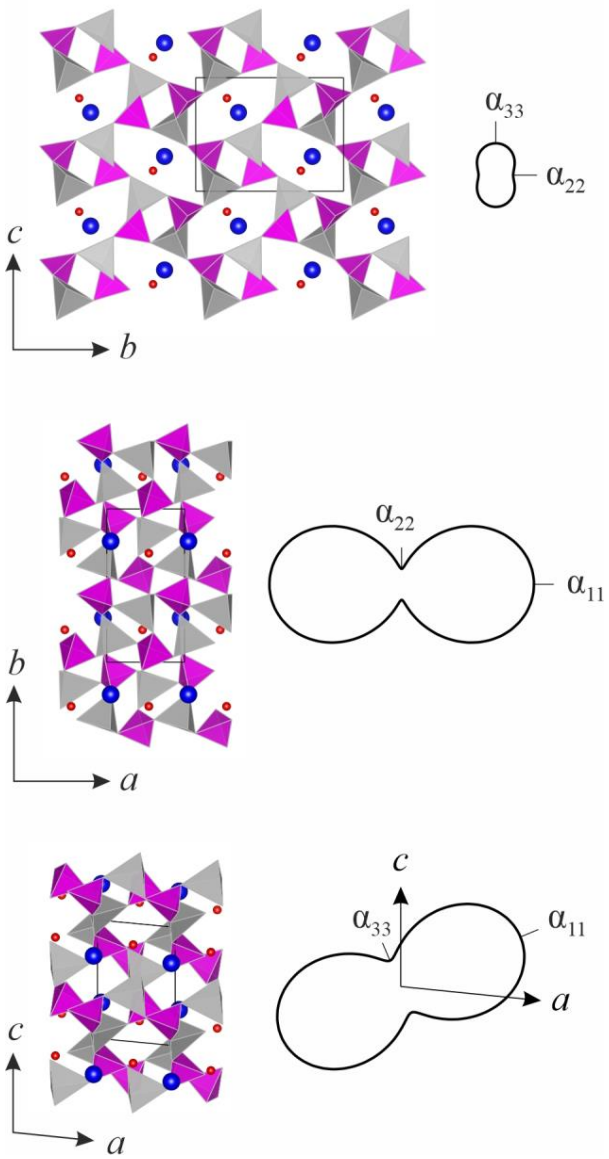

Figure 6. Crystal structure of $BaAs_2Zn_2O_8 \cdot H_2O$ with the section of thermal deformations. AsO_4 and ZnO_4 tetrahedra are given in purple and grey, respectively. Ca and O atoms are presented as blue and red spheres, respectively. *a*, *b* and *c* denote the crystallographic axes, α_{11}, α_{22} and α_{33} show the thermal expansion coefficients along crystal-physical axes.

The volume thermal expansion of $BaAs_2Zn_2O_8 \cdot H_2O$ (α_V = 21 $\times$ 10^{-6} °C^{-1}) is very close to the mean value of the volume thermal expansion of the feldspar-related natural and synthetic compounds with feldspar topology (<α_V> = 20 $\times$ 10^{-6} °C^{-1}, calculated

on the base of 27 different compounds from Henderson [48]). The thermal expansion of feldspar-related compounds with paracelsian topology is studied in less detail. As far as we know, only the danburite group of minerals [46] and slawsonite [49] have been studied under high-temperature conditions. Their $<\alpha_V> = 22 \times 10^{-6}$ °C^{-1}, calculated on the base of four compounds, is very close to the thermal expansion of compounds with feldspar topology.

Little is known about the high-temperature behavior of compounds containing Zn, As and O as the main structural constituents. Among them, only adamite, $Zn_2(AsO_4)(OH)$, has been studied under high-temperature conditions [50]. The volume thermal expansion of adamite equals 34×10^{-6} °C^{-1} and is more intense than of $BaAs_2Zn_2O_8 \cdot H_2O$. The extension of ZnO_6 octahedra dimers is the main cause of the expansion [50]. ZnO_6 octahedra undergo a sharp distortion during heating, whereas other crystal structure components (ZnO_5 trigonal bipyramids and AsO_4 tetrahedra) behave as quite rigid units.

The character of the thermal deformations of any compounds depends on their symmetry and topology, whereas the deformations value depends on chemical composition and topology [51]. Nevertheless, each compound has some individual features of the thermal deformations that allow the groups with isostructural compounds to be divided into subgroups. The studied high-temperature behavior of $BaAs_2Zn_2O_8 \cdot H_2O$ is one more example confirming this thesis.

4. Discussion

According to the International Mineralogical Association (IMA) List of Minerals, only 66 minerals containing Zn, As and O are known to date (Table 3). The crystal structures of these minerals usually contain As, coordinated by four oxygen atoms (tetrahedral coordination), but there are some arsenide minerals, where As is present in trigonal coordination. Simultaneously, the Zn atom can be surrounded by four, five or six O atoms. Consequently, these minerals could be considered as zincoarsenites ($ZnO_4 + AsO_3$), zincoarsenates ($ZnO_4 + AsO_4$), zinc arsenates ($ZnO_5/ZnO_6 \pm ZnO_4 + AsO_4 \pm AsO_3$), and more complex compounds, whose crystal structures include ZnO_n (n = 4, 5, 6), $AsOm$ (m = 3, 4) and other polyhedra, e.g., FeO_6, PO_4, CO_3, SiO_4, TeO_3, etc. The majority of these 66 minerals adopt framework structures (36 minerals); layered structures comprise a quarter (19), whereas minerals with chains structures are rare (3). The crystal structure of eight of them is either not determined or yet to be published (Table 3). Interestingly, crystal structures containing only isolated ZnO_4- and AsO_4-groups are unknown.

Table 3. List of minerals containing ZnO_n (n = 4, 5, 6) and AsO_n (n = 3, 4) polyhedra.

Mineral Name	Chemical Formula	Structural Motif	Reference
	$ZnO–As_2O_3$ System		
Reinerite	$^{[4]}Zn_3(^{[3]}AsO_3)_2$	Framework	[52]
Leiteite	$^{[4]}Zn^{[3]}As_2O_4$	Layers	[53,54]
	$ZnO–As_2O_5–H_2O$ System		
Adamite	$^{[5]}Zn^{6]}Zn(^{[4]}AsO_4)(OH)$	Framework	[55]
Arsenohopeite	$^{[6]}Zn^{[4]}Zn_2(^{[4]}AsO_4)_2 \cdot 4H_2O$	Framework	[56]
Cardite	$^{[4]}Zn_{5.5}(^{[4]}AsO_4)_2(^{[4]}AsO_3OH)(OH)_3 \cdot 3H_2O$	Framework	[57]
Davidlloydite	$^{[6]}Zn^{[4]}Zn_2(^{[4]}AsO_4)_2 \cdot 4H_2O$	Framework	[58]
Koritnigite	$^{[6]}Zn(^{[4]}AsO_3OH) \cdot H_2O$	Layers	[59]
Köttigite	$^{[6]}Zn_3(^{[4]}AsO_4)_2 \cdot 8H_2O$	Layers	[60]
Ianbruceite	$^{[5]}Zn^{[6]}ZnO[^{[4]}AsO_3(OH)](H_2O)_{3.53}$	Layers	[61]
Legrandite	$^{[5]}Zn^{[6]}Zn(^{[4]}AsO_4)(OH) \cdot H_2O$	Framework	[55,62]
Paradamite	$^{[5]}Zn_2(^{[4]}AsO_4)(OH)$	Framework	[55]
Warikahnite	$^{[4]}Zn^{[5]}Zn_2^{[6]}Zn_3(^{[4]}AsO_4)_4 \cdot 4H_2O$	Framework	[63]
	$K_2O–ZnO–As_2O_3$ System		
Filatovite	$K^{[4]}(Al,Zn)_2^{[4]}(As,Si)_2O_8$	Framework	[15]
Pharmazincite	$K^{[4]}Zn^{[4]}AsO_4$	Framework	[64]

Table 3. *Cont.*

Mineral Name	Chemical Formula	Structural Motif	Reference
	PbO–ZnO–As_2O_5–H_2O System		
Arsenbrackebuschite	$Pb_2(Fe,^{[6]}Zn)(^{[4]}AsO_4)_2(OH,H_2O)$	Chains	[65]
Arsendescloizite	$Pb^{[6]}Zn(^{[4]}AsO_4)(OH)$	Framework	[66]
Feinglosite	$Pb_2Zn(AsO_4)_2{\cdot}H_2O$	No structure	[67]
Helmutwinklerite	$Pb^{[6]}Zn_2(^{[4]}AsO_4)_2{\cdot}2H_2O$	Layers	[68]
Tsumcorite	$Pb^{[6]}Zn_2(^{[4]}AsO_4)_2{\cdot}2H_2O$	Layers	[69]
Zincgartrellite	$Pb^{[6]}Zn_2(^{[4]}AsO_4)_2(H_2O,OH)_2$	Layers	[70]
	CaO–ZnO–As_2O_5–H_2O System		
Austinite	$Ca\ ^{[6]}Zn(\ ^{[4]}AsO_4)(OH)$	Framework	[71,72]
Gaitite	$Ca_2{}^{[6]}Zn(^{[4]}AsO_4)_2{\cdot}2H_2O$	Chains	[73]
Lotharmeyerite	$Ca\ ^{[6]}Zn_2(\ ^{[4]}AsO_4)_2{\cdot}2H_2O$	Framework	[74]
Prosperite	$Ca_2{}^{[6]}Zn_4(^{[4]}AsO_4)_4{\cdot}H_2O$	Framework	[75]
Stergiouite	$Ca^{[4]}Zn_2(^{[4]}AsO_4)_2{\cdot}4H_2O$	Framework	[76]
Zincroselite	$Ca_2{}^{[6]}Zn(^{[4]}AsO_4)_2{\cdot}2H_2O$	Chains	[73]
	CuO–ZnO–As_2O_5–H_2O and CuO–ZnO–As_2O_5 Systems		
Arsenoveszelyite	$Cu_2{}^{[4]}Zn(^{[4]}AsO_4)(OH)_3{\cdot}2H_2O$	Layers	[77]
Goldhillite	$Cu_5{}^{[4]}Zn(^{[4]}AsO_4)_2(OH)_6{\cdot}H_2O$	Layers	[78]
Sabelliite	$Cu_2{}^{[4],[6]}Zn(\ ^{[4]}AsO_4)(OH)_3$	Framework	[79,80]
Stranskiite	$Cu^{[5]}Zn_2(^{[4]}AsO_4)_2$	Framework	[81,82]
Theisite	$Cu_5Zn_5(AsO_4)_2(OH)_{14}$	No structure	[83]
Veselovskite	$^{[6]}ZnCu_4(^{[4]}AsO_4)_2(^{[4]}AsO_3OH)_2{\cdot}9H_2O$	Framework	[84]
Zincolivenite	$Cu^{[5]}Zn(^{[4]}AsO_4)(OH)$	Framework	[85]
	Fe_2O_3–ZnO–As_2O_5–H_2O System		
Mapimite	$^{[6]}Zn_2Fe_3(^{[4]}AsO_4)_3(OH)_4{\cdot}10H_2O$	Framework	[86]
Metaköttigite	$(^{[6]}Zn,Fe)_3(^{[4]}AsO_4)_2{\cdot}8(H_2O,OH)$	Layers	[87]
Ojuelaite	$^{[6]}ZnFe_2(^{[4]}AsO_4)_2(OH)_2{\cdot}4H_2O$	Framework	[88]
Wilhelmkleinite	$^{[6]}\ ZnFe_2(^{[4]}AsO_4)_2(OH)_2$	Framework	[89]
	Other Minerals Containing ZnO_n and AsO_n Polyhedra		
Arakiite	$^{[4]}ZnMn_{12}Fe_2(^{[3]}AsO_3)(^{[4]}AsO_4)_2(OH)_{23}$	Layers	[90,91]
Chlorophoenicite	$(Mn,Mg,^{[6]}Zn)_3{}^{[4]}Zn_2(^{[4]}AsO_4)(OH,O)_6$	Layers	[92]
Claraite	$(Cu,^{[5],[6]}Zn)_{15}(CO_3)_4(^{[4]}AsO_4)_2(SO_4)(OH)_{14}{\cdot}7H_2O$	Layers	[93]
Cuprozheshengite	$Pb_4CuZn_2(AsO_4)_2(PO_4)_2(OH)_2$	No structure	[94]
Dugganite	$Pb_3{}^{[4]}Zn_3(TeO_6)(^{[4]}AsO_4)_2$	Framework	[95]
Ekatite	$(Fe,Fe,^{[4]}Zn)_{12}(^{[4]}AsO_3)_6(^{[4]}AsO_3,SiO_3OH)_2(OH)_6$	Framework	[96]
Erikapohlite	$(\square_{0.5}Cu_{0.5})CuCa^{[6]}Zn_2(^{[4]}AsO_4)_3{\cdot}H_2O$	Framework	[97]
Eurekadumpite	$(Cu,Zn)_{16}(TeO_3)_2(AsO_4)_3Cl(OH)_{18}{\cdot}7H_2O$	Layers(?)	[98]
Fahleite	$CaZn_5Fe_2(AsO_4)_6{\cdot}14H_2O$	No structure	[99]
Ferrilotharmeyerite	$CaZn^{[6]}Fe(^{[4]}AsO_4)_2(OH){\cdot}H_2O$	Layers	[68]
Gerdtremmelite	$ZnAl_2(AsO_4)(OH)_5$	No structure	[100]
Holdenite	$Mn_6{}^{[4]}Zn_3(^{[4]}AsO_4)_2(SiO_4)(OH)_8$	Framework	[101]
Jamesite	$Pb_2{}^{[6]}ZnFe_2(Fe,^{[6]}Zn)_4(^{[4]}AsO_4)_4(OH)_8(OH,O)_2$	Framework	[102]
Joelbruggerite	$Pb_3{}^{[4]}Zn_3Sb^{[4]}As_2O_{13}(OH)$	Framework	[103]
Keyite	$(\square_{0.5}Cu_{0.5})CuCd^{[6]}Zn_2(^{[4]}AsO_4)_3{\cdot}H_2O$	Framework	[104]
Kolicite	$^{[4]}Zn_4Mn^{2+}{}_7(^{[4]}AsO_4)_2(SiO_4)_2(OH)_8$	Framework	[105]
Kolitschite	$Pb[^{[5]}Zn_{0.5},\square_{0.5}]Fe_3(^{[4]}AsO_4)_2(OH)_6$	Framework	[106]
Kraisslite	$^{[4]}Zn_3(Mn,Mg)_{25}(Fe,Al)(^{[3]}AsO_3)_2[(Si,^{[4]}As)O_4]_{10}(OH)_{16}$	Framework	[107]
Magnesiochlorophoenicite	$Mg_3{}^{[4]}Zn_2(^{[4]}AsO_4)(OH,O)_6$	Layers	[108]
Mcgovernite	$^{[4]}Zn_3(Mn,Mg,Fe,Al)_{42}(^{[3]}AsO_3)_2(^{[4]}AsO_4)_4[(Si,^{[4]}As)O_4]_8(OH)_{42}$	Layers	[109]
Metalodèvite	$Zn(UO_2)_2(AsO_4)_2{\cdot}10H_2O$	No structure	[110]
Nyholmite	$Cd_3{}^{[6]}Zn_2(^{[4]}AsO_3OH)_2(^{[4]}AsO_4)_2{\cdot}4H_2O$	Framework	[111]
Odanielite	$Na\square^{[6]}Zn^{[6]}Zn_2(^{[4]}AsO_4)[^{[4]}AsO_3(OH)]_2$	Framework	[112,113]
Ogdensburgite	$Ca_2Fe_4Zn(AsO_4)_4(OH)_6{\cdot}6H_2O$	No structure (layers?)	[114]
Philipsburgite	$Cu_5{}^{[4]}Zn(^{[4]}AsO_4)(PO_4)(OH)_6{\cdot}H_2O$	Framework	[115]
Puttapaite	$Pb_2Mn_2ZnCr_4O_2(AsO_4)_4(OH)_6{\cdot}12H_2O$	No structure	[116]
Wiklundite	$Pb_2(Mn,^{[6]}Zn)_3(Fe,Mn)_2(Mn,Mg)_{19}(^{[3]}AsO_3)_2[(Si,^{[4]}As)O_4]_6(OH)_{18}Cl_6$	Layers	[117]
Zheshengite	$Pb_4ZnZn_2(AsO_4)_2(PO_4)_2(OH)_2$	No structure	[118]
Zincobradaczekite	$NaCuCu^{[6]}Zn_2(^{[4]}AsO_4)_3$	Framework	[113,119,120]

There are only two natural zincoarsenites: reinerite, $Zn_3(AsO_3)_2$ [52] and leiteite, $ZnAs_2O_4$ [53,54]. Both were found in the oxidation zone of the famous lead-zinc-copper

Tsumeb mine (Namibia) and were probably formed at lower (<50 °C) temperature conditions [54]. Similarly, only two natural zincoarsenates are known: filatovite $K(Al,Zn)_2(As,Si)_2O_8$ and pharmazincite $KZnAsO_4$. As mentioned above, filatovite belongs to the feldspar group of minerals [15], whereas pharmazincite is isostructural with nepheline, i.e., it is part of the feldspathoid group minerals [64]. Both are found only in one place with very specific geological conditions, namely in the fumaroles of the Tolbachik volcano, Kamchatka, Russia [13,64]. It is supposed that pharmazincite is deposited from the gas phase at a temperature above 360 °C [64], whereas the temperature of the filatovite formation is most probably above 500 °C [119].

There are no natural anhydrous zinc arsenates ($ZnO–As_2O_5$ system). In the $ZnO–As_2O_5–H_2O$ system, there are two hydroxyl and eight hydrated zinc arsenate minerals (Table 3). However, none of them contain Zn in exclusively tetrahedral coordination. Legrandite, adamite, paradamite and warikahnite crystallize as the framework structures [55,62,63], while ianbruceite, koritnigite and köttigite adopt layered structures [59–61]. Arsenohopeite and davidlloydite are sheet structures with infinite sheets of tetrahedra linked by interlayer octahedral sites [56,58]. As in cardite, H_2O is bonded to the structural unit in each of these structures [57], except for ianbruceite, which contains interstitial H_2O groups [61]. All of the minerals mentioned above can be found as the supergene phases that are typical for the oxidation zones of polymetallic deposits, such as Tsumeb (Namibia) or Broken Hill (Australia).

Zinc arsenates (and zinc arsenate-arsenites) comprise a large group of 52 minerals, which contain ZnO_n (n = 4, 5, 6) and AsO_m (m = 3, 4) polyhedra. Almost half of them belongs to $PbO–ZnO–As_2O_5–H_2O$ (six minerals), $CaO–ZnO–As_2O_5–H_2O$ (six minerals), $CuO–ZnO–As_2O_5–H_2O$ (six minerals) and $Fe_2O_3–ZnO–As_2O_5–H_2O$ (four minerals) systems (Table 3). The remaining 30 minerals have a more complex chemical composition and cannot be easily divided into separate groups. It should be noted that the vast majority of the minerals containing Zn and As are hydrous, i.e., contain (OH) or H_2O groups. According to the IMA list of minerals, there are only seven anhydrous zinc arsenate minerals: dugganite, filatovite, leiteite, pharmazincite, reinerite, stranskiite and zincobradaczekite, whereas duggianite can contain a small amount of (OH) groups [121]. Three of the six remaining anhydrous minerals (filatovite, pharmazincite and zincobradaczekite) are formed in specific geological conditions, such as fumaroles on the Tolbachik volcano, Kamchatka, Russia, i.e., they are formed under high-temperature conditions (above 350 °C) directly from gas [119]. Leiteite and reinerite, as mentioned above, are zinc arsenides and, as a consequence, there is only one anhydrous zinc arsenate mineral—stranskiite, which was first described by Strunz [122] from the oxidation zone in the Tsumeb mine, Africa, but is also known on the Tolbachik volcano [119].

It should be separately highlighted that among all 66 minerals there are only 12 containing Zn and As in exclusively tetrahedral coordination: cardite, dugganite, ekatite, filatovite, goldhillite, holdenite, joelbruggerite, kolicite, magnesiochlorophoenicite, pharmazincite, philipsburgite and stergiouite. Five-fold coordinated Zn is known for nine minerals only: adamite, claraite, ianbruceite, kolitschite, lengradite, paradamite, stranskiite, warikahnite and zincolivenite. Thus, most of the minerals contain Zn in octahedral coordination. Additionally, arakiite, mcgovemite and wiklundite can be mentioned as minerals containing As in both trigonal and tetrahedral coordination.

The crystals of $BaAs_2Zn_2O_8·H_2O$ were obtained at 120–220 °C and a moderate acidity (pH = 6), whereas $BaAs_2Zn_2O_8$ was obtained during both the synthesis and heating of $BaAs_2Zn_2O_8·H_2O$ to 150–300 °C. Considering the above, both $BaAs_2Zn_2O_8·H_2O$ and $BaAs_2Zn_2O_8$ can also be found in nature. Their formation can be realized in very specific geological conditions, such as volcanic fumaroles or the oxidation zones of polymetallic deposits.

5. Conclusions

The high-temperature behavior of $BaAs_2Zn_2O_8·H_2O$ was studied using single-crystal X-ray diffraction and hot-stage Raman spectroscopy. It undergoes a phase transition

as the temperature increases with the formation of the anhydrous phase ($BaAs_2Zn_2O_8$), which is clearly defined using both methods by abrupt changes of the Raman bands' position and unit-cell parameters. This process is accompanied by an increase in symmetry. The difference between two phases is in the channel occupancy: it could be occupied by H_2O groups and/or Ba atoms. However, both crystal structures have the similar topology of a three-dimensional framework of AsO_4 and ZnO_4 tetrahedra. Generally, the thermal expansion of the initial phase is similar to other feldspar-related compounds with paracelsian topology. However, it has an extremely anisotropic character that can be caused by the "preparation" of the crystal structure for the dehydration process and following phase transition. It is assumed that both hydrous and anhydrous phases can be found in nature, but for their formation, very specific geological conditions are needed.

Supplementary Materials: The CIF-files at all temperature points are available online at https://www.mdpi.com/article/10.3390/min12101262/s1.

Author Contributions: L.A.G. wrote the original manuscript; L.A.G. and O.S.V. obtained the high-temperature X-ray diffraction data; D.V.P. obtained the Raman spectra at room temperature; O.S.V. and V.N.B. obtained the Raman spectra under high-temperature conditions; L.A.G. performed crystal structure calculations and Raman spectra processing; T.Đ. provided the studied sample and made a significant contribution to writing the discussion section of the manuscript. The manuscript was written through contributions made by all authors. All authors have read and agreed to the published version of the manuscript.

Funding: This research was funded by the Russian Science Foundation, grant number 22-77-10033 (to L.A.G. and O.S.V.).

Data Availability Statement: Not applicable.

Acknowledgments: The authors thank the X-ray Diffraction Centre of the Resource Centre of Saint Petersburg State University for providing instrumental and computational resources. The Raman measurements were performed at the Centre for Geo-Environmental Research and Modelling (GEOMODEL) and the center for optical and laser materials research of Research Park, Saint Petersburg State University.

Conflicts of Interest: The authors declare no conflict of interest.

References

1. Smith, J.V.; Brown, W.L. *Feldspar Minerals. Crystal Structures, Physical, Chemical and Microstructural Properties*; Springer Verlag: Berlin/Heidelberg, Germany, 1988; Volume 1, 828 p.
2. Parsons, I. *Feldspars and Their Reactions*; Kluwer Academic Publishers: Amsterdam, The Netherlands, 1994; 650 p.
3. Deer, W.A.; Howie, R.A.; Zusmann, J. *Rock-Forming Minerals. Framework Silicates: Feldspars*; The Geological Society: London, UK, 2001; Volume 4A, 973 p.
4. Bokij, G.B.; Borutsky, B.E. Minerals. Framework Silicates, Issue 1. In *Silicates with Broken Frameworks. Feldspars*; Nauka: Moscow, Russia, 2003; Volume 1, 583 p. (In Russian)
5. Pakhomova, A.; Simonova, D.; Koemets, I.; Koemets, E.; Aprilis, G.; Bykov, M.; Gorelova, L.; Fedotenko, T.; Prakapenka, V.; Dubrovinsky, L. Polymorphism of feldspars above 10 GPa. *Nat. Comm.* **2020**, *11*, 2721. [CrossRef]
6. Pakhomova, A.S.; Bykova, E.; Bykov, M.; Glazyrin, K.; Gasharova, B.; Liermann, H.-P.; Mezouar, M.; Gorelova, L.A.; Krivovichev, S.V.; Dubrovinsky, L. Closer look into close packing: Pentacoordinated silicon in the high-pressure polymorph of danburite. *IUCrJ* **2017**, *4*, 671–677. [CrossRef]
7. Pakhomova, A.; Aprilis, G.; Bykov, M.; Gorelova, L.; Krivovichev, S.; Belov, M.P.; Abrikosov, I.A.; Dubrovinsky, L. Penta- and hexa-coordinated beryllium and phosphorous in high-pressure modifications of $CaBe_2P_2O_8$. *Nat. Comm.* **2019**, *10*, 2800. [CrossRef]
8. Gorelova, L.A.; Pakhomova, A.S.; Krivovichev, S.V.; Dubrovinsky, L.S.; Kasatkin, A.V. High pressure phase transitions of paracelsian $BaAl_2Si_2O_8$. *Sci. Rep.* **2019**, *9*, 12652. [CrossRef]
9. Gorelova, L.A.; Pakhomova, A.S.; Krzhizhanovskaya, M.G.; Winkler, B.; Krivovichev, S.V.; Dubrovinsky, L.S. Pressure-induced phase transitions in danburite-type borosilicates. *J. Phys. Chem. C* **2020**, *124*, 26048–26061. [CrossRef]
10. Gorelova, L.A.; Pakhomova, A.S.; Krzhizhanovskaya, M.G.; Pankin, D.V.; Krivovichev, S.V.; Dubrovinsky, L.S.; Kasatkin, A.V. Crystal structure evolution of slawsonite $SrAl_2Si_2O_8$ and paracelsian $BaAl_2Si_2O_8$ upon compression and decompression. *J. Phys. Chem. C* **2021**, *125*, 13014–13023. [CrossRef]

11. Gorelova, L.; Pakhomova, A.; Aprilis, G.; Yin, Y.; Laniel, D.; Winkler, B.; Krivovichev, S.; Pekov, I.; Dubrovinskia, N.; Dubrovinsky, L.S. Edge-sharing BO_4 tetrahedra and penta-coordinated silicon in the high-pressure modification of $NaBSi_3O_8$. *Inorg. Chem. Front.* **2022**, *9*, 1735–1742. [CrossRef]
12. Krivovichev, S.V. Feldspar polymorphs: Diversity, complexity, stability. *Zap. Ross. Mineral. Obshch.* **2020**, *149*, 16–66. [CrossRef]
13. Vergasova, L.P.; Krivovichev, S.V.; Britvin, S.N.; Burns, P.C.; Ananiev, V.V. Filatovite, $K[(Al,Zn)_2(As,Si)_2O_8]$, a new mineral species from the Tolbachik volcano, Kamchatka peninsula, Russia. *Eur. J. Mineral.* **2004**, *16*, 533–536. [CrossRef]
14. Shchipalkina, N.V.; Pekov, I.V.; Britvin, S.N.; Koshlyakova, N.N.; Sidorov, E.G. Arsenic and phosphorus in feldspar framework: Sanidine–filatovite solid solution series from fumarolic exhalations of the Tolbachik volcano, Kamchatka, Russia. *Phys. Chem. Minerals.* **2020**, *47*, 1. [CrossRef]
15. Filatov, S.K.; Krivovichev, S.V.; Burns, P.C.; Vergasova, L.P. Crystal structure of filatovite, $K[(Al,Zn)_2(As,Si)_2O_8]$, the first arsenate of the feldspar group. *Eur. J. Mineral.* **2004**, *16*, 537–543. [CrossRef]
16. Bolotina, N.B.; Rastsvetaeva, R.K.; Kashaev, A.A. Refinement of the twinned structure of cymrite from the Ruby Creek deposit (Alaska). *Crystallogr. Rep.* **2010**, *55*, 569–574. [CrossRef]
17. Fasshauer, D.W.; Chatterjee, N.D.; Marler, B. Synthesis, structure, thermodynamic properties, and stability relations of K-cymrite, $K[AlSi_3O_8]\cdot H_2O$. *Phys. Chem. Miner.* **1997**, *24*, 455–462. [CrossRef]
18. Zhang, R.Y.; Liou, Y.G.; Iizuka, Y.; Yang, J.S. First record of K-cymrite in North Qaidam UHP eclogite, Western China. *Am. Mineral.* **2009**, *94*, 222–228. [CrossRef]
19. Mikhno, A.O.; Schmidt, U.; Korsakov, A.V. Origin of K-cymrite and kokchetavite in the polyphase mineral inclusions from Kokchetav UHP calc-silicate rocks: Evidence from confocal Raman imaging. *Eur. J. Mineral.* **2013**, *25*, 807–816. [CrossRef]
20. Romanenko, A.V.; Rashchenko, S.V.; Sokol, A.G.; Korsakov, A.V.; Seryotkin, Y.V.; Glazyrin, K.V.; Musiyachenko, K. Crystal structures of K-cymrite and kokchetavite from single-crystal X-ray diffraction. *Am. Mineral.* **2021**, *106*, 404–409. [CrossRef]
21. Đorđević, T. $Ba(ZnAsO_4)_2\cdot H_2O$, a non-centrosymmetric framework structure related to feldspar. *Eur. J. Mineral.* **2011**, *23*, 437–447. [CrossRef]
22. Smedley, P.L.; Kinniburgh, D.G. A review of the source, behaviour and distribution of arsenic in natural waters. *Appl. Geochem.* **2002**, *17*, 517–568. [CrossRef]
23. Miretzky, P.; Cirelli, A.F. Remediation of arsenic-contaminated solid by iron amendments: A review. *Crit. Rev. Environ. Sci. Technol.* **2010**, *40*, 93–115. [CrossRef]
24. Smith, E.; Naidu, R.; Alston, A.M. Arsenic in the soils environment: A review. *Adv. Agron.* **1998**, *64*, 149–195.
25. Agilent. *CrysAlis PRO*; Agilent Technologies: Yarnton, UK, 2012.
26. Sheldrick, G.M. A short history of SHELX. *Acta Crystallogr. A* **2008**, *64*, 112. [CrossRef] [PubMed]
27. Bubnova, R.S.; Firsova, V.A.; Filatov, S.K. Software for determining the thermal expansion tensor and the graphic representation of its characteristic surface (Theta to Tensor-TTT). *Glass Phys. Chem.* **2013**, *39*, 347–350. [CrossRef]
28. Lucas, F.; Elfakir, A.; Wallez, G.; Quarton, M. Synthesis and Rietveld refinement of new phosphate and arsenate analogues of paracelsian. *Can. Mineral.* **1998**, *36*, 1045–1051.
29. Lucas, F.; Elfakir, A.; Quarton, M. X-ray powder diffraction data of $A^{II}(ZnX^{V}O_4)_2$ compounds (A = Sr, Ba; X = P, As). *Powder Diffr.* **1999**, *14*, 222–230. [CrossRef]
30. Izatulina, A.; Gurzhiy, V.; Frank-Kamenetskaya, O. Weddellite from renal stones: Structure refinement and dependence of crystal chemical features on H_2O content. *Am. Mineral.* **2014**, *99*, 2–7. [CrossRef]
31. Mills, S.J.; Christy, A.G. The Great Barrier Reef Expedition 1828–29: The crystal structure and occurrence of weddellite, ideally $CaC_2O_4\cdot 2.5H_2O$, from the Low Isles, Queensland. *Mineral. Mag.* **2016**, *80*, 399–406. [CrossRef]
32. Curetti, N.; Pastero, L.; Bernasconi, D.; Cotellucci, A.; Corazzai, I.; Archetti, M.; Pavese, A. Thermal stability of calcium oxalates from CO_2 sequestration for storage purposes: An in situ HT-XRPD and TGA combined study. *Minerals* **2022**, *12*, 53. [CrossRef]
33. Britvin, S.N.; Krzhizhanovskaya, M.G.; Zolotarev, A.A.; Gorelova, L.A.; Obolonskaya, E.V.; Vlasenko, N.S.; Shilovskikh, V.V.; Murashko, M.N. Crystal chemistry of schreibersite, $(Fe,Ni)_3P$. *Am. Mineral.* **2021**, *106*, 1520–1529. [CrossRef]
34. Dollimore, D.; Griffiths, D.L. Differential thermal analysis study of various oxalates in oxygen and nitrogen. *J. Therm. Anal. Calorim.* **1970**, *2*, 229–250. [CrossRef]
35. Kutaish, N.; Aggarwal, P.; Dollimore, D. Thermal analysis of calcium oxalate samples obtained by various preparative routes. *Thermochim. Acta.* **1997**, *297*, 131–137. [CrossRef]
36. Pastero, L.; Curetti, N.; Ortenzi, M.A.; Schiavoni, M.; Destefanis, E.; Pavese, A. CO_2 capture and sequestration in stable Ca-oxalate, via Ca-ascorbate promoted green reaction. *Sci. Total Environ.* **2019**, *666*, 1232–1244. [CrossRef] [PubMed]
37. Frost, R.L.; Weier, M.L. Thermal treatment of whewellite—A thermal analysis and Raman spectroscopic study. *Thermochim. Acta.* **2004**, *409*, 79–85. [CrossRef]
38. Szekely, T.; Varhegyi, G.; Till, F.; Szabo, P.; Jakab, E. The effects of heat and mass transport on the results of thermal decomposition studies: Part 1. The three reactions of calcium oxalate monohydrate. *J. Anal. Appl. Pyrolysis.* **1987**, *11*, 71–81. [CrossRef]
39. Price, D.; Dollimore, D.; Fatemi, N.; Whitehead, R. Mass spectrometric determination of kinetic parameters for solid state decomposition reactions. Part 1. Method; calcium oxalate decomposition. *Thermochim. Acta.* **1980**, *42*, 323–332. [CrossRef]
40. Kloprogge, T.; Boström, T.E.; Weier, M.L. In situ observation of the thermal decomposition of weddelite by heating stage environmental scanning electron microscopy. *Am. Miner.* **2004**, *89*, 245–248. [CrossRef]

41. Windig, W.; Kistemaker, P.; Haverkamp, J.; Meuzelaar, H. The effects of sample preparation, pyrolysis and pyrolyzate transfer conditions on pyrolysis mass spectra. *J. Anal. Appl. Pyrolysis* **1979**, *1*, 39–52. [CrossRef]
42. Anderson, E.M.; Ericsson, I. Thermal degradation of organic polymers using different metals as the pyrolysis filament. *J. Anal. Appl. Pyrolysis* **1981**, *3*, 35–47. [CrossRef]
43. Yeates, R.M.; Harrison, W.T.A. Synthesis, crystal structure and properties of $Na_3Zn_4O(AsO_4)_3{\cdot}6H_2O$, a new framework zincoarsenate. *J. Mater. Chem.* **2002**, *12*, 1103–1106. [CrossRef]
44. Wiggin, S.B.; Weller, M.T. A chiral, 16-ring channels framework and a layered caesium zincoarsenate. *Chem. Commun.* **2006**, 1100–1102. [CrossRef]
45. Megaw, H.D. The architecture of feldspars. In *The Feldsparsi*; MacKenzie, W.S., Zussman, J., Eds.; NATO Advanced Study Institute, 1972; Manchester University Press: Manchester, UK, 1974; pp. 2–24.
46. Gorelova, L.A.; Filatov, S.K.; Krzhizhanovskaya, M.G.; Bubnova, R.S. High-temperature behavior of danburite-like-borosilicates $MB_2Si_2O_8$ (*M* = Ca, Sr, Ba). *Phys. Chem. Glasses.* **2015**, *56*, 189–196.
47. Sleight, A.W. Thermal Contraction. *Endeavor* **1995**, *19*, 64–68. [CrossRef]
48. Henderson, C.M.B. Composition, thermal expansion and phase transitions in framework silicates: Revisitation and review of natural and synthetic analogues of nepheline-, feldspar- and leucite-mineral groups. *Solids* **2021**, *2*, 1–49. [CrossRef]
49. Gorelova, L.A.; Vereshchagin, O.S.; Kasatkin, A.V. Thermal Expansion and Polymorphism of Slawsonite $SrAl_2Si_2O_8$. *Minerals* **2022**, *11*, 1150. [CrossRef]
50. Zema, M.; Tarantino, S.C.; Boiocchi, M.; Callegari, A.M. Crystal structure of adamite at high temperature. *Mineral. Mag.* **2016**, *80*, 901–914. [CrossRef]
51. Filatov, S.K. *Vysokotemperaturnaya Kristallokhimiya. Teoriya, Metody I Rezul'taty Issledovanii*; (High-temperature crystal chemistry: Theory, methods and results of investigations); Nedra: Leningrad, Russia, 1990; p. 289. (In Russian)
52. Geier, B.H.; Weber, K. Reinerit $Zn_3[AsO_3]_2$, ein neues Mineral der Tsumeb Mine Südwestafrika. *Neues Jahrb. Mineral. Monatsh.* **1958**, *1958*, 160–167.
53. Cesbron, F.P.; Erd, R.C.; Czamanski, G.K.; Vachey, H. Leiteite: A new mineral from Tsumeb. *Mineral. Rec. Tsumeb Issue* **1977**, 95–97.
54. Ghose, S.; Sen Gupta, P.K.; Schlemper, E.O. Leiteite, $ZnAs_2O_4$: A novel type of tetrahedral layer structure with arsenite chains. *Am. Mineral.* **1987**, *72*, 629–632.
55. Jinnouchi, S.; Yoshiasa, A.; Sugiyama, K.; Shimura, R.; Arima, H.; Momma, K.; Miyawaki, R. Crystal structure refinements of legrandite, adamite, and paradamite: The complex structure and characteristic hydrogen bonding network of legrandite. *J. Mineral. Petrol. Sci.* **2016**, *111*, 35–43. [CrossRef]
56. Neuhold, F.; Kolitsch, U.; Bernhardt, H.-J.; Lengauer, C.L. Arsenohopeite, a new zinc arsenate mineral from the Tsumeb mine, Namibia. *Mineral. Mag.* **2012**, *76*, 603–612. [CrossRef]
57. Elliott, P. Cardite, $Zn_{5.5}(AsO_4)_2(AsO_3OH)(OH)_3{\cdot}3H_2O$, a new zinc arsenate mineral from Broken Hill, New South Wales, Australia. *Mineral. Petrol.* **2021**, *115*, 467–475. [CrossRef]
58. Hawthorne, F.C.; Cooper, M.A.; Abdu, Y.A.; Ball, N.A.; Back, M.E.; Tait, K.T. Davidlloydite, ideally $Zn_3(AsO_4)_2(H_2O)_4$, a new arsenate mineral from the Tsumeb mine, Otjikoto (Oshikoto) region, Namibia: Description and crystal structure. *Mineral. Mag.* **2012**, *76*, 45–57. [CrossRef]
59. Keller, P.; Hess, H.; Riffel, H. Die Kristallstruktur von Koritnigit, $Zn[H_2O\,|\,HOAsO_3]$. *Neues Jahrb. Mineral. Monatsh.* **1980**, *138*, 316–332.
60. Yoshiasa, A.; Miyano, Y.; Isobe, H.; Sugiyama, K.; Arima, H.; Nakatsuka, A.; Momma, K.; Miyawaki, R. Structural refinement of köttigite–parasymplesite solid solution: Unique cation site occupancy and chemical bonding with water molecules. *J. Mineral. Petrol. Sci.* **2016**, *111*, 363–369. [CrossRef]
61. Cooper, M.A.; Abdu, Y.A.; Ball, N.A.; Hawthorne, F.C.; Back, M.E.; Tait, K.T.; Schlüter, J.; Malcherek, T.; Pohl, D.; Gebhard, G. Ianbruceite, ideally $[Zn_2(OH)(H_2O)(AsO_4)](H_2O)_2$, a new arsenate mineral from the Tsumeb mine, Otjikoto (Oshikoto) region, Namibia: Description and crystal structure. *Mineral. Mag.* **2012**, *76*, 1119–1131. [CrossRef]
62. Hawthorne, F.C.; Abdu, Y.A.; Tait, K.T. Hydrogen bonding in the crystal structure of legrandite: $Zn_2(AsO_4)(OH)(H_2O)$. *Can. Mineral.* **2013**, *51*, 233–241. [CrossRef]
63. Riffel, H.; Keller, P.; Hess, H. Die Kristallstruktur von Warikahnit, $Zn_3[(H_2O)_2\,|\,(AsO_4)_2]$. *Tscher. Miner. Petrog. Mitteilungen.* **1980**, *27*, 187–199. [CrossRef]
64. Pekov, I.V.; Yapaskurt, V.O.; Belakovsky, D.I.; Vigasina, M.F.; Zubkova, N.V.; Sidorov, E.G. New arsenate minerals from the Arsenatnaya fumarole, Tolbachik volcano, Kamchatka, Russia. VII. Pharmazincite, $KZnAsO_4$. *Mineral. Mag.* **2017**, *81*, 1001–1008. [CrossRef]
65. Hofmeister, W.; Tillman, E. Strukturelle untersuchungen an arsenbrackebuschit. *TMPM* **1978**, *25*, 153–163. [CrossRef]
66. Keller., P.; Lissner, F.; Schleid, T. The crystal structure of arsendescloizite $PbZn(OH)[AsO_4]$, from Tsumeb (Namibia). *Neues Jahrb. Mineral. Monatsh.* **2003**, 374–384. [CrossRef]
67. Clark, A.M.; Criddle, A.J.; Roberts, A.C.; Bonardi, M.; Moffatt, E.A. Feinglosite, a new mineral related to brackebuschite, from Tsumeb, Namibia. *Mineral. Mag.* **1997**, *61*, 285–289. [CrossRef]
68. Krause, W.; Belendorff, K.; Bernhardt, H.J.; McCammon, C.A.; Effenberger, H.; Mikenda, W. Crystal chemistry of the tsumcorite-group minerals. New data on ferrilotharmeyerite, tsumcorite, thometzekite, mounanaite, helmutwinklerite, and a redefinition of gartrellite. *Eur. J. Mineral.* **1998**, *10*, 179–206. [CrossRef]

69. Tillmanns, E.; Gebert, W. The crystal structure of tsumcorite, a new mineral from the Tsumeb Mine, S.W. Africa. *Acta Crystallogr.* **1973**, *B29*, 2789–2794. [CrossRef]
70. Effenberger, H.; Krause, W.; Bernhardt, H.J.; Martin, M. On the symmetry of tsumcorite group minerals based on the new species rappoldite and zincgartrellite. *Mineral. Mag.* **2000**, *64*, 1109–1126. [CrossRef]
71. Clark, L.A.; Pluth, J.J.; Steele, I.; Smith, J.V.; Sutton, S.R. Crystal structure of austinite, $CaZn(AsO_4)OH$. *Mineral. Mag.* **1997**, *61*, 677–683. [CrossRef]
72. Giuseppetti, G.; Tadini, C. The crystal structure of austinite, $CaZn(AsO_4)(OH)$, from Kamareza, Laurion (Greece). *Neues Jahrb. Mineral. Monatsh.* **1988**, 159–166.
73. Keller, P.; Lissner, F.; Schleid, T. The crystal structures of zincroselite and gaitite: Two natural polymorphs of $Ca_2Zn[AsO_4]_2 \cdot 2H_2O$ from Tsumeb, Namibia. *Eur. J. Mineral.* **2004**, *16*, 353–359. [CrossRef]
74. Yang, Y.W.; Evans, S.H.; Downs, R.T.; Yang, H. Lotharmeyerite, $Ca(Zn,Mn)_2(AsO_4)_2(H_2O,OH)_2$. *Acta Crystallogr.* **2012**, *E68*, i9–i10. [CrossRef]
75. Keller, P.; Riffel, H.; Hess, H. Die kristallstruktur von prosperit, $Ca_2Zn_4[H_2O\,|\,(AsO_4)_4]$. *Z. Kristallogr.* **1982**, *158*, 33–42. [CrossRef]
76. Rieck, B.; Giester, G.; Lengauer, C.L.; Chanmuang, C.N.; Topa, D. Stergiouite, $CaZn_2(AsO_4)_2 \cdot 4H_2O$—A new mineral from the Lavrion Mining District, Greece. *Mineral. Petrol.* **2020**, *114*, 319–327. [CrossRef]
77. Shen, H.; Hao, J.; Sun, N.; Li, G.; Xue, Y.; Luo, L. Arsenoveszelyite, IMA 2021-076a, in CNMNC Newsletter 66. *Eur. J. Mineral.* **2022**, *34*, 253. [CrossRef]
78. Ismagilova, R.M.; Rieck, B.; Kampf, A.R.; Giester, G.; Zhitova, E.S.; Lengauer, C.L.; Krivovichev, S.V.; Zolotarev, A.A.; Ciesielczuk, J.; Mikhailova, J.A.; et al. Goldhillite, $Cu_5Zn(AsO_4)_2(OH)_6 \cdot H_2O$, a new mineral species, and redefinition of philipsburgite, $Cu_5Zn[(AsO_4)(PO_4)](OH) \cdot H_2O$, as an As–P ordered species. *Mineral. Mag.* **2022**, *86*, 436–446. [CrossRef]
79. Olmi, F.; Santucci, A.; Trosti-Ferroni, R. Sabelliite, a new copper-zinc arsenate-antimonate mineral from Sardinia, Italy. *Eur. J. Mineral.* **1995**, *7*, 1325–1330. [CrossRef]
80. Olmi, F.; Sabelli, C.; Trosti-Ferroni, R. The crystal structure of sabelliite. *Eur. J. Mineral.* **1995**, *7*, 1331–1337. [CrossRef]
81. Plieth, K.; Sanger, G. Die struktur des stranskiite $Zn_2Cu(AsO_4)_2$. *Z. Kristallogr.* **1967**, *124*, 91–100. [CrossRef]
82. Calvo, C.; Leung, K.Y. Refinement of the structure of stranskiite. *Z. Kristallogr.* **1969**, *130*, 231–233. [CrossRef]
83. Williams, S.A. Theisite, a new mineral from Colorado. *Mineral. Mag.* **1982**, *46*, 49–50. [CrossRef]
84. Sejkora, J.; Ondruš, P.; Novák, M. Veselovskýite, triclinic $(Zn,Cu,Co)Cu_4(AsO_4)_2(AsO_3OH)_2 \cdot 9H_2O$, a Zn-dominant analogue of lindackerite. *Neues Jahrb. Mineral. Abhandl.* **2010**, *187*, 83–90. [CrossRef]
85. Chukanov, N.V.; Pushcharovsky, D.Y.; Zubkova, N.V.; Pekov, I.V.; Pasero, M.; Merlino, S.; Möckel, S.; Rabadanov, M.K.; Belakovskiy, D.I. Zincolivenite $CuZn(AsO_4)(OH)$: A new adamite-group mineral with ordered distribution of Cu and Zn. *Doklady Earth Sci.* **2007**, *415*, 841–845. [CrossRef]
86. Ginderow, D.; Cesbron, F. Structure de la mapimite, $Zn_2Fe_3(AsO_4)_3(OH)_4 \cdot 10H_2O$. *Acta Crystallogr.* **1981**, *B37*, 1040–1043. [CrossRef]
87. Schmetzer, K.; Amthauer, G.; Stähle, V.; Medenbach, O. Metaköttigit, $(Zn,Fe^{3+})(Zn,Fe^{3+},Fe^{2+})_2(AsO_4)_2 \cdot 8(H_2O,OH)$, ein neues Mineral aus Mapimi, Mexiko. *Neues Jahrb. Mineral. Monatsh.* **1982**, 506–518.
88. Hughes, J.M.; Bloodaxe, E.S.; Kobel, K.D. The atomic arrangement of ojuelaite, $ZnFe^{3+}{}_2(AsO_4)_2(OH)_2 \cdot 4H_2O$. *Mineral. Mag.* **1996**, *60*, 519–521. [CrossRef]
89. Adiwidjaja, G.; Friese, K.; Klaska, K.H.; Moore, P.B.; Schlüter, J. The crystal structure of the new mineral wilhelmkleinite $ZnFe^{3+}{}_2(OH)_2(AsO_4)_2$. *Z. Kristallogr.* **2000**, *215*, 96–101. [CrossRef]
90. Cooper, M.A.; Hawthorne, F.C. Local Pb^{2+}–□ disorder in the crystal structure of jamesite, $Pb_2ZnFe^{3+}{}_2(Fe^{3+}{}_{2.8}Zn_{1.2})(AsO_4)_4(OH)_8[(OH)_{1.2}O_{0.8}]$, and revision of the chemical formula. *Can. Mineral.* **1999**, *37*, 53–60.
91. Roberts, A.C.; Grice, J.D.; Cooper, M.A.; Hawthorne, F.C.; Feinglos, M.N. Arakiite, a new Zn-bearing hematolite-like mineral from Långban, Värmland, Sweden. *Mineral. Rec.* **2000**, *31*, 253–256.
92. Moore, P.B. The crystal structure of chlorophoenicite. *Am. Mineral.* **1968**, *53*, 1110–1119.
93. Biagioni, C.; Orlandi, P. Claraite, $(Cu,Zn)_{15}(AsO_4)_2(CO_3)_4(SO_4)(OH)_{14} \cdot 7H_2O$: Redefinition and crystal structure. *Eur. J. Mineral.* **2017**, *29*, 1031–1044. [CrossRef]
94. Sun, N.; Grey, I.E.; Li, G.; Rewitzer, C.; Xue, Y.; Mumme, W.G.; Shen, H.; Hao, J.; MacRae, C.M.; Riboldi Tunnicliffe, A.; et al. Cuprozheshengite, IMA 2021-095a, in: CNMNC Newsletter 67. *Eur. J. Mineral.* **2022**, *34*, 359. [CrossRef]
95. Lam, A.E.; Groat, L.A.; Ercit, T.S. The crystal structure of dugganite, $Pb_3Zn_3Te^{6+}As_2O_{14}$. *Can. Mineral.* **1998**, *36*, 823–830.
96. Keller, P. Ekatite, $(Fe^{3+},Fe^{2+},Zn)_{12}(OH)_6[AsO_3]_6[AsO_3,HOSiO_3]_2$, a new mineral from Tsumeb, Nambia, and its crystal structure. *Eur. J. Mineral.* **2001**, *13*, 769–777. [CrossRef]
97. Schlüter, J.; Malcherek, T.; Mihailova, B.; Gebhard, G. The new mineral erikapohlite, $Cu_3(Zn,Cu,Mg)_4Ca_2(AsO_4)_6 \cdot 2H_2O$, the Ca-dominant analogue of keyite, from Tsumeb, Namibia. *Neues Jahrb. Mineral. Abhandl.* **2013**, *190*, 319–325. [CrossRef]
98. Pekov, I.V.; Chukanov, N.V.; Zadov, A.E.; Roberts, A.C.; Jensen, M.C.; Zubkova, N.V.; Nikischer, A.J. Eurekadumpite $(Cu,Zn)_{16}(TeO_3)_2(AsO_4)_3Cl(OH)_{18} \cdot 7H_2O$—A new hypergene mineral. *Zap. Ross. Mineral. Obsh.* **2010**, *139*, 26–35.
99. Medenbach, O.; Schmetzer, K.; Abraham, K. Fahleite from Tsumeb/Namibia, a new mineral belonging to the smolianinovite group. *Neues Jahrb. Mineral. Monatsh.* **1988**, *4*, 167–171.
100. Schmetzer, K.; Medenbach, O. Gerdtremmelite, $(Zn,Fe)(Al,Fe)_2[(AsO_4)\,|\,(OH)_5]$, a new mineral from Tsumeb, Namibia. *Neues Jahrb. Mineral. Monatsh.* **1985**, *1*, 1–6.

101. Moore, P.B.; Araki, T. Holdenite, a novel cubic close-packed structure. *Am. Mineral.* **1977**, *62*, 513–521.
102. Cooper, M.A.; Hawthorne, F.C. The effect of differences in coordination on ordering of polyvalent cations in close-packed structures: The crystal structure of arakiite and comparison with hematolite. *Can. Mineral.* **1999**, *37*, 1471–1482.
103. Mills, S.J.; Kolitsch, U.; Miyawaki, R.; Groat, L.A.; Poirier, G. Joelbruggerite, $Pb_3Zn_3(Sb^{5+},Te^{6+})As_2O_{13}(OH,O)$, the Sb^{5+} analog of dugganite, from the Black Pine mine, Montana. *Am. Mineral.* **2009**, *94*, 1012–1017. [CrossRef]
104. Cooper, M.A.; Hawthorne, F.C. The crystal structure of keyite, $Cu^{2+}{}_3(Zn,Cu^{2+})_4Cd_2(AsO_4)_6(H_2O)_2$, an oxysalt mineral with essential cadium. *Can. Mineral.* **1996**, *34*, 623–630.
105. Peacor, D.R. The crystal structure of kolicite, $Mn_7(OH)_4[As_2Zn_4Si_2O_{16}(OH)_4]$. *Am. Mineral.* **1980**, *65*, 483–487.
106. Grey, I.E.; Mumme, W.G.; Bordet, P. A new crystal-chemical variation of the alunite-type structure in monoclinic $PbZn_{0.5}Fe_3(AsO_4)_2(OH)_6$. *Can. Mineral.* **2008**, *46*, 1355–1364. [CrossRef]
107. Cooper, M.A.; Hawthorne, F.C. Crystal structure of kraisslite, $Zn_3(Mn,Mg)_{25}(Fe^{3+},Al)(As^{3+}O_3)_2[(Si,As^{5+})O_4]_{10}(OH)_{16}$, from the Sterling Hill mine, Ogdensburg, Sussex County, New Jersey, USA. *Mineral. Mag.* **2012**, *76*, 2819–2836. [CrossRef]
108. Dunn, P.J. Magnesium-chlorophoenicite redefined and new data on chlorophoenicite. *Can. Mineral.* **1981**, *19*, 333–336.
109. Hawthorne, F.C. Long-range and short-range cation order in the crystal structures of carlfrancisite and mcgovernite. *Mineral. Mag.* **2018**, *82*, 1101–1118. [CrossRef]
110. Plášil, J.; Sejkora, J.; Čejka, J.; Škácha, P.; Goliáš, V.; Ederová, J. Characterization of phosphate-rich metalodèvite from Príbram, Czech Republic. *Can. Mineral.* **2010**, *48*, 113–122. [CrossRef]
111. Elliott, P.; Turner, P.; Jensen, P.; Kolitsch, U.; Pring, A. Description and crystal structure of nyholmite, a new mineral related to hureaulite, from Broken Hill, New South Wales, Australia. *Mineral. Mag.* **2009**, *73*, 723–735. [CrossRef]
112. Keller, P.; Hess, H. Die Kristallstrukturen von O'Danielit, $Na(Zn,Mg)_3H_2(AsO_4)_3$, und Johillerite, $Na(Mg,Zn)_3Cu(AsO_4)_3$. *Neues Jahrb. Mineral. Monatsh.* **1988**, *9*, 395–404.
113. Hatert, F. A new nomenclature scheme for the alluaudite supergroup. *Eur. J. Mineral.* **2019**, *31*, 807–822. [CrossRef]
114. Dunn, P.J. Ogdensburgite a new calcium-zinc-ferric iron arsenate mineral from Sterling Hill, New Jersey. *Mineral. Rec.* **1981**, *12*, 369–370.
115. Peacor, D.R.; Dunn, P.J.; Ramik, R.A.; Sturman, B.D.; Zeihen, L.G. Philipsburgite, a new copper zinc arsenate hydrate related to kipushite, from Montana. *Can. Mineral.* **1985**, *23*, 255–258.
116. Elliott, P.; Kampf, A.R. Puttapaite, IMA 2020-025. CNMNC Newsletter No. 56. *Mineral. Mag.* **2020**, *84*, 623–627. [CrossRef]
117. Cooper, M.A.; Hawthorne, F.C.; Langhof, J.; Hålenius, U.; Holtstam, D. Wiklundite, ideally $Pb_2[4](Mn^{2+},Zn)_3(Fe^{3+},Mn^{2+})_2(Mn^{2+},Mg)_{19}(As^{3+}O_3)_2[Si,As^{5+})O_4]_6(OH)_{18}Cl_6$, a new mineral from Långban, Filipstad, Värmland, Sweden: Description and crystal structure. *Mineral. Mag.* **2017**, *81*, 841–855. [CrossRef]
118. Li, G.; Sun, N.; Shen, H.; Xue, Y.; Hao, J. Zheshengite, IMA 2022-011, in CNMNC Newsletter 67. *Eur. J. Mineral.* **2022**, *34*, 359–364. [CrossRef]
119. Pekov, I.V.; Koshlyakova, N.N.; Zubkova, N.V.; Lykova, I.S.; Britvin, S.N.; Yapaskurt, V.O.; Agakhanov, A.A.; Shchipalkina, N.V.; Turchkova, A.G.; Sidorov, E.G. Fumarolic arsenates–A special type of arsenic mineralization. *Eur. J. Mineral.* **2018**, *30*, 305–322. [CrossRef]
120. Pekov, I.V.; Lykova, I.; Koshlyakova, N.N.; Belakovskiy, D.I.; Vigasina, M.F.; Turchkova, A.G.; Britvin, S.N.; Sidorov, E.G.; Scheidl, K.S. A new mineral species zincobradaczekite, $NaCuCuZn_2(AsO_4)_3$, and a new isomorphous series bradaczekite-zincobradaczekite in the alluaudite group. *Phys. Chem. Mineral.* **2020**, *47*, 36. [CrossRef]
121. Williams, S.A. Khinite, parakhinite, and dugganite, three new tellurates from Tombstone, Arizona. *Am. Mineral.* **1978**, *63*, 1016–1019.
122. Strunz, H. Stranskiit, ein neues Mineral. *Sci. Nat.* **1960**, *47*, 376. [CrossRef]